Insight into the Relationship Between Viscosity and Structure of $CaO-SiO_2-MgO-Al_2O_3$ Molten Slags

ZIWEI CHEN, HAO WANG, YONGQI SUN, LILI LIU, and XIDONG WANG

This article elucidates the quantitative relationship between viscosity and structure in a basic slag system of $CaO-SiO_2-MgO-Al_2O_3$ and focuses on the role of Al_2O_3. Slag viscosity was measured by the rotating cylinder method, and structural information was obtained using Fourier transformation infrared, Raman and magic angular spinning nuclear magnetic resonance (MAS-NMR) techniques. The results show that, as the Al_2O_3 content increased, slag viscosity increased initially and decreased afterwards, directly indicating that Al_2O_3 had an amphoteric effect on slag viscosity. The Raman spectra verified that with increasing Al_2O_3 content, the concentrations of Q^0(Si) and Q^2(Si) decreased first and then increased, while that of Q^1(Si) kept increasing and that of Q^3(Si) increased first and then decreased. The ^{27}Al MAS-NMR spectra proved that the mole ratios of AlO_5 and AlO_6 to AlO_4 kept increasing with the increase of Al_2O_3 content, and, overall, Al_2O_3 changed from a network former to a network modifier. The relationship between the viscosity and structure of the molten slags was further analyzed quantitatively based on the modified (NBO/T), denoted as (NBO/T)′, and we found a fine linear correlation between the logarithm of viscosity and (NBO/T)′. Moreover, the variations of thermodynamic properties of this system also indirectly supported the present experimental results.

https://doi.org/10.1007/s11663-019-01660-7

I. INTRODUCTION

In recent years, the iron ore grade has been gradually declining with continuous depletion of ore reserves. It is estimated that most iron ores mined in China contain < 30 wt pct iron, which is far below the global average (60 wt pct iron).[1] In this situation, relatively high-degree iron ores from India and Australia have been considered alternative options.[2] A typical character of these ores is a higher Al_2O_3 content.[3,4] In addition, many changes in the operational conditions of blast furnaces have taken place in China, including the utilization of low-cost non-metallurgical coals.[5] As a result, the Al_2O_3 concentration in molten slags has increased to > 20 wt pct.[6] This composition change of slag will significantly affect its thermophysical properties, such as the viscosity and crystallization behaviors.

Slag viscosity is a fundamental thermophysical property and plays an important role in metallurgical processes.[7] It is sensitive to compositional variation of slag melt. In fact, the variational composition impacts viscosity, relying on the change in structure at the micro-level, that is, slag viscosity is directly related to the structure of the slag melt. From the micro-level, viscosity reflects the internal friction between molecules of a fluid when they flow under external force. The internal friction is determined by parameters such as the structure of the molecules and the interaction forces between the molecules. Thus, a deep understanding of the origin of slag viscosity at the micro-level is highly necessary.

Generally, blast furnace slags are considered a mixture of oxides, mainly composed of CaO, SiO_2, MgO, Al_2O_3 and other minor elements. Therefore, $CaO-SiO_2-MgO-Al_2O_3$ is commonly considered a basic quaternary system of slags.[8] In terms of the role of oxides in the melt structure, CaO and MgO are network modifiers; SiO_2 is a network former; Al_2O_3 is an intermediate oxide with the ability to polymerize or depolymerize networks,[9–11] and its amphoteric behavior on the structure and viscosity is complicated, and some unclear issues remain.

Many investigations[12–17] focused on the lower end concentration of Al_2O_3 and failed to discover its amphoteric behavior. For example, the thermophysical properties and structure of $CaO-SiO_2-MgO-Al_2O_3$ slag

ZIWEI CHEN, HAO WANG, LILI LIU, and XIDONG WANG are with the Department of Energy and Resources Engineering, College of Engineering, Peking University, 100871 Beijing, P.R. China. Contact e-mail: xidong@pku.edu.cn YONGQI SUN is with the School of Chemical Engineering, The University of Queensland, Brisbane QLD 4072, Australia. Contact e-mail: uqysun16@uq.edu.au
Manuscript submitted April 9, 2019.
Article published online August 22, 2019.

Table I. Chemical Compositions of Modified Slags (in Mass Pct)

Samples	CaO	SiO_2	MgO	Al_2O_3	Basicity	Primary Crystalline Phase	Liquidus Temperature (°C)
A1							
Designed	43.5	43.5	8	5	1	$Ca_2MgSi_2O_7$ or $Ca_3MgSi_2O_8$	1356
XRF	44.39	42.94	7.28	4.78	1.03		
A2							
Designed	41	41	8	10	1	$Ca_3MgSi_2O_8$	1331
XRF	42.35	39.71	7.18	9.11	1.06		
A3							
Designed	38.5	38.5	8	15	1	$Ca_3MgSi_2O_8$	1288
XRF	39.48	38.03	7.24	13.72	1.04		
A4							
Designed	36	36	8	20	1	$Ca_2Al_2SiO_7$	1356
XRF	37.93	35.73	7.34	18.25	1.06		
A5							
Designed	33.5	33.5	8	25	1	$Ca_2Al_2SiO_7$	1400
XRF	34.38	32.80	7.14	24.52	1.05		

have been studied previously[17] and showed that, with increasing Al_2O_3 content, the slag viscosity increased and Al_2O_3 dominantly acted as a network former. A few other studies[18–20] found a distinguishing phenomenon. For example, Park *et al.*[20] explored the viscosity of CaO-SiO_2-Al_2O_3 slag and found that the viscosity increased at the initial stage of Al_2O_3 addition and then switched over to decrements at higher Al_2O_3 content. However, the viscous flow behaviors were discussed only based on a simple structural analysis using Fourier transformation infrared (FTIR) spectra. So far, the investigations into the amphoteric behavior of Al_2O_3 on slag viscosity were still insufficient and unclear. In fact, the dependence of viscosity upon the structure of melts has been widely acknowledged.[17–20] To clearly understand the amphoteric behavior of Al_2O_3, it is essential to quantitatively investigate the viscosity and structural characteristics of molten slags. This was the aim of the present study.

In the present work, a basic slag system of CaO-SiO_2-MgO-Al_2O_3 was prepared, and its viscosity was measured by the rotating cylinder method. Its structure was characterized first qualitatively using FTIR, Raman and magic angular spinning nuclear magnetic resonance (MAS-NMR) techniques. The relationship between viscosity and structure was further quantitatively analyzed based on the degree of polymerization (DOP) of the network. The DOP was quantified by a structural parameter, namely, $(NBO/T)'$, where NBO is the number of non-bridging oxygen and T is the number of network former. $(NBO/T)'$ can be calculated from the fitting results of Raman and MAS-NMR spectra using Gaussian functions. The functional relation between the logarithm of viscosity and $(NBO/T)'$ was established based on a linear fitting method. Furthermore, three important thermodynamic properties of the system, namely, activity coefficients, molar Gibbs free energy of real mixing and molar excess Gibbs free energy, were employed to deepen these discussions.

II. EXPERIMENTAL PROCEDURE

A. *Sample Preparation*

In this study, the modified slags of the CaO-SiO_2-MgO-Al_2O_3 system were prepared with a fixed binary basicity (mass ratio of CaO to SiO_2), using analytically pure (AR) CaO (99.9 pct), SiO_2 (99.8 pct), MgO (99.9 pct) and Al_2O_3 (99.9 pct) [produced by Alfa Aesar (China) Company]. The chemical compositions of designed samples are listed in Table I. The compositions were also represented by the red arrow on the ternary phase diagram of the CaO-SiO_2-(8 wt pct) MgO-Al_2O_3 system in Figure 1, which was calculated from Factsage 7.1 (Thermfact/CRCT, Canada, and GTT-Technologies, Germany). The primary crystalline phases and liquidus temperatures of the five designed samples were obtained from the phase diagram and are summarized in Table I.

Two hundred grams of the mixed powders of oxides was placed in a molybdenum (Mo) crucible ($\Phi 40 \times H180$ mm) and then premelted at 1540 °C for 2 hours in a tube furnace under high-purity Ar atmosphere to homogenize the slag melts. Subsequently, the molten slags were quickly poured into water and quenched to a glassy state. Finally, the obtained samples were dried at 110 °C in a drying oven and crushed to powders < 300 meshes for structure and viscosity measurements.

The prepared samples were analyzed by X-ray fluoroscopy (XRF) and X-ray diffraction (XRD), as shown in Table I and Figure 2, respectively. The XRF values presented a small deviation from the designed values of samples, and the XRD results verified the amorphous nature of the prepared samples.

B. *Viscosity Measurement*

The viscosities of slag melts were determined by the rotating cylinder method with a Brookfield digital viscometer instrument (model LVDV-II+; Brookfield Engineering Laboratories, Middleboro, MA). The

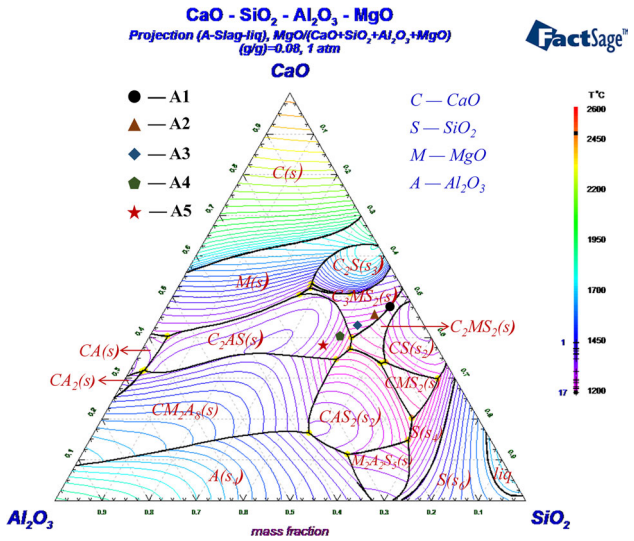

Fig. 1—Ternary phase diagram of the CaO-SiO_2-(8 wt pct) MgO-Al_2O_3 slag system.

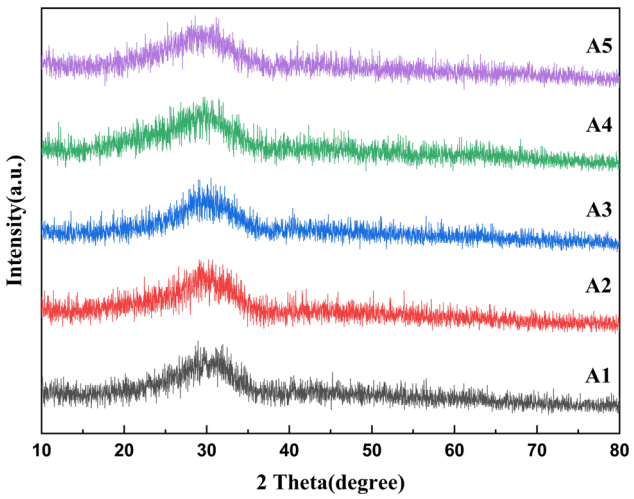

Fig. 2—XRD results of the prepared glassy samples.

details of the experimental apparatus, including the schematic diagram and dimensions of the spindle, crucible and shaft, are displayed in Figure 3. It should be pointed out that the parts (crucible, spindle and shaft) in touch with melts were made by molybdenum (Mo). The molybdenum oxide contents in the samples before and after viscosity measurement were analyzed by XRF, and they were in the range of 0.14 to 0.43 wt pct. The molybdenum oxide contents and their changes before and after viscosity measurement were very small. Hence, the effect of Mo on the viscosity measurement can be ignored.

In the process of viscosity measurement, first the viscometer was calibrated using standard silicone oils with known viscosities at room temperature. Then, 140 g of prepared glassy sample was loaded into a Mo crucible, and the Mo crucible fitted inside a high-pure graphite crucible was placed in the even temperature zone of the resistance furnace. High-purity Ar gas (0.3 L/min) was used to protect the Mo crucible, spindle and shaft from oxidization during the experiment. The sample temperature was raised to the peak temperature of 1540 °C and then held for > 2 hours at this temperature to homogenize the melt. The viscosity of the melt was first measured at 1540 °C until its values varied within 2.5 pct when the shaft rotating speed changed. Then, the viscosities of the melt were measured and recorded during continuous cooling with a cooling rate of 5 °C/min and a fixed shaft rotating speed of 200 r/min

C. *Spectral Measurements*

In this study, FTIR, Raman and MAS-NMR techniques were employed to analyze the structure of the glassy samples. First, for FTIR tests, sample aliquots of 2 mg with 200 mg of KBr were mixed and ground in an agate mortar and pressed into 13.0-mm-diameter discs. An IR spectrophotometer (Tensor 27, Bruker, Germany) equipped with a KBr detector was used, and the absorption spectra in the range of 400 to 4000 cm^{-1} were recorded with 2 cm^{-1} resolution. Second, the Raman spectra in the range of 200 to 2000 cm^{-1} were obtained using a laser confocal Raman spectrometer (JY-T64000, Jobin-Yvon Company, France). The tests were operated at room temperature with the light source of a 1-mW semiconductor and an excitation wavelength of 532 nm. Finally, to further identify the structural roles of Al in the glassy samples, ^{27}Al MAS-NMR tests of sample powders were performed on a solid-state FT-NMR spectrometer (Avance III 400M, Bruker, Germany) using an MAS probe of a 4-mm ZrO_2 rotor and two pairs of DuPont Vespel caps.

III. RESULTS AND DISCUSSION

A. *The Viscosities of CaO-SiO_2-MgO-Al_2O_3 Molten Slags*

The slag viscosity measured during continuous cooling is exhibited in Figure 4(a). As expected, the viscosity kept increasing smoothly with decreasing temperature until it reached the crystallization temperature, which could be concluded from the inflection point of the viscosity curve. It could be clearly observed that the crystallization temperatures of samples with 5 and 10 wt pct Al_2O_3 content were about 1350 °C and 1335 °C, respectively, which was basically in line with the liquidus temperatures of 1356 °C and 1331 °C shown in Table I. However, the exact crystallization temperatures of samples with higher Al_2O_3 content were not clear in these experiments. It was interesting to note that there was a crossing point between the viscosity curves of samples with 20 and 25 wt pct Al_2O_3 contents, and the temperature of the crossing point was close to the liquidus temperature of the latter. Also, the phase diagram showed that the crystallization temperature of the latter sample was higher. Hence, it could be explained that the lower viscosity at high temperature created a suitable melt environment that was in favor of

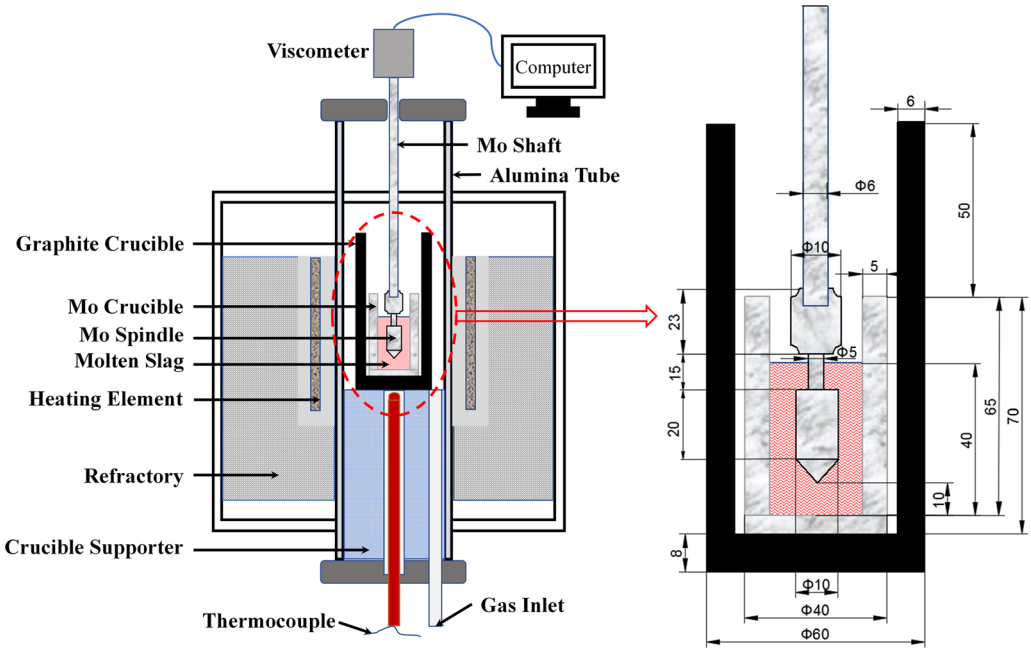

Fig. 3—Schematic diagram of the experimental apparatus for the measurement of slag viscosity (unit: mm).

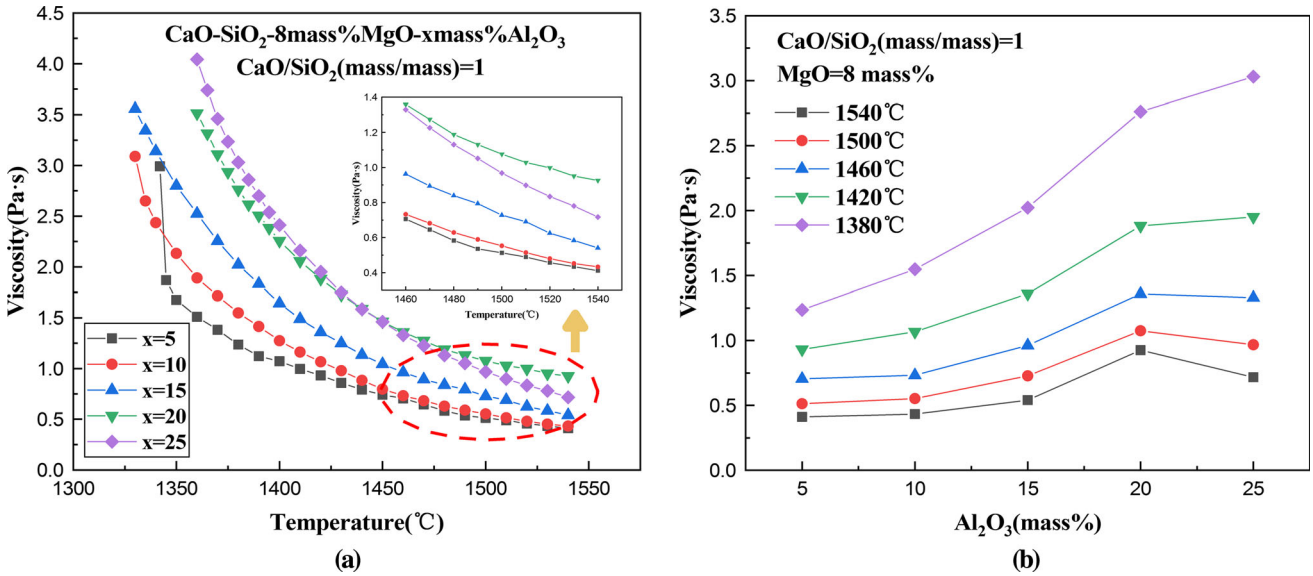

Fig. 4—Viscosity changes of CaO-SiO_2-(8 wt pct) MgO-Al_2O_3 slags (*a*) with the temperature; (*b*) with the Al_2O_3 content at the fixed basicity of 1.

the movement and rearrangement of ion clusters. Nevertheless, the formation of a regular structure resembling a crystal lattice, even tiny grains, in turn, would significantly increase the melt viscosity. Essentially, this phenomenon was analogous but less obvious compared with the intersecting viscosity curves of samples with 5 and 10 wt pct Al_2O_3 content.

To more directly understand the influence of Al_2O_3 content on viscosity, the variation trend of viscosity with incremental Al_2O_3 content at different temperatures of 1540 °C, 1500 °C, 1460 °C, 1420 °C and 1380 °C is displayed in Figure 4(b). As shown, two types of variation trends existed. Under the condition of temperature > 1460 °C, the viscosity increased first, followed by a decrease with increasing Al_2O_3 content, and a maximum value occurred as the Al_2O_3 content was 20 wt pct. At lower temperatures, the viscosity kept increasing, and the effect of Al_2O_3 on viscosity was more pronounced. Hence, it could be inferred that Al_2O_3 had an amphoteric effect on the viscosity of slags at high temperatures, and its role gradually transformed from an acidic oxide to a basic oxide, but when the temperature was lower, the role of Al_2O_3 became more complex because of the crystallization behaviors.

B. *Microstructural Analysis of the Slags*

1. *FTIR and Raman spectra*

The FTIR absorption spectra in the region of 400 to 1300 cm^{-1} of glassy samples are shown in Figure 5(a). As can be noted, all spectra exhibited three broad absorption bands: a low frequency band from 400 to 600 cm^{-1}, an intermediate frequency band from 600 to 800 cm^{-1} and a high frequency band from 800 to 1200 cm^{-1}, with each containing different structural information.[21,22] Generally, the low-frequency band from 400 to 600 cm^{-1} was primarily related to the Si-O_b-Si bending (O_b denotes bridging oxygen), Ca-O_{nb} and Mg-O_{nb} stretching vibrations (O_{nb} denotes non-bridging oxygen). The center of 400 to 600 cm^{-1} was ascribed to the Ca-O_{nb} and Mg-O_{nb} stretching vibrations, while the wave shoulder at approximately 450 cm^{-1} was ascribed to Si-O_b-Si bending vibrations.[23–25] The intensity of Ca-O_{nb} and Mg-O_{nb} stretching vibrations was higher than Si-O_b-Si bending vibrations because infrared spectra were more sensitive to asymmetric structures.[24] Also, the band located at the intermediate frequency of 600 to 800 cm^{-1} originated from the Si-O_b symmetry stretching vibrations, and the most intense absorption band at the high frequency band from 800 to 1200 cm^{-1} was attributed to the stretching vibrations of Si-O_{nb} in variational types of SiO_4 tetrahedra.[26–28] With the Al_2O_3 concentration increasing, it could be observed that Si-O_b-Si bending, Ca-O_{nb} and Mg-O_{nb} stretching, and Si-O_b symmetry stretching vibrations became less pronounced because the contents of CaO and SiO_2 simultaneously decreased; also, the position of the high frequency band (800 to 1200 cm^{-1}) related to SiO_4 tetrahedra shifted toward a lower wavenumber, which was because of the coupling vibrations of Si-O_{nb} and ^{IV}Al-O when the vibration force constant of ^{IV}Al-O was smaller.[29]

Raman spectra were complementary to verify the FTIR spectra results and obtain more quantitative structural information on five species of SiO_4 tetrahedra, which are conventionally expressed as Q^i(Si) (i = 0, 1, 2, 3 and 4), i representing the number of bridging oxygens per coordinated Si atom. Figure 5(b) depicts the Raman spectra in the region of 300 to 1300 cm^{-1} of these glassy samples. Similar to the FTIR spectra, the entire Raman spectra were also traditionally divided into three typical regions: the low frequency region (200 to 600 cm^{-1}), intermediate frequency region (600 to 800 cm^{-1}) and the high frequency region (800 to 1200 cm^{-1}). The low and intermediate frequency regions (200 to 800 cm^{-1}) were associated with motions of bridging oxygen in the network, *i.e.*, bending vibrations of T-O_b-T and stretching vibrations of T-O_b (T represents Si or Al atoms), while the high-frequency region (800 to 1200 cm^{-1}) was connected to the characteristic motions of SiO_4 tetrahedra.[11,30]

As Figure 5(b) clearly shows, with increasing Al_2O_3 content, two peaks at ~ 350 and ~ 700 cm^{-1}, assigned to the Si-O_b-Si bending and Si-O_b symmetry stretching vibrations, respectively, gradually faded away, which corresponded to the FTIR results. However, the peak positioned at 580 cm^{-1}, attributed to the bending vibrations of Si-O_b-Al, became more pronounced with increasing Al_2O_3 content, which could be explained as follows. First, Al atoms inserted into networks would increase with additional Al_2O_3 added. Second, the Al atoms introduced into the network preferentially formed Si-O_b-Al (residual charge of − 0.25) bonds with SiO_4 tetrahedra rather than Al-O_b-Al (residual charge of − 0.5) bonds because of the more facile charge compensation of the former, which was also named aluminum avoidance,[31,32] so the Si-O_b-Al bending vibrations would become significantly enhanced. Simultaneously, for this reason, the Si-O_b-Si framework became diminished and the Si-O_b-Si bending and Si-O_b symmetry stretching vibrations became weaker. As for the broad band associated with SiO_4 tetrahedra at the high-frequency region, it moved slightly to a lower frequency range, which was consistent with the FTIR results. In more detail, two obvious peaks could be observed at ~ 870 and ~ 950 cm^{-1} in sample A1, and a new coupling peak appeared at ~ 920 cm^{-1} as the Al_2O_3

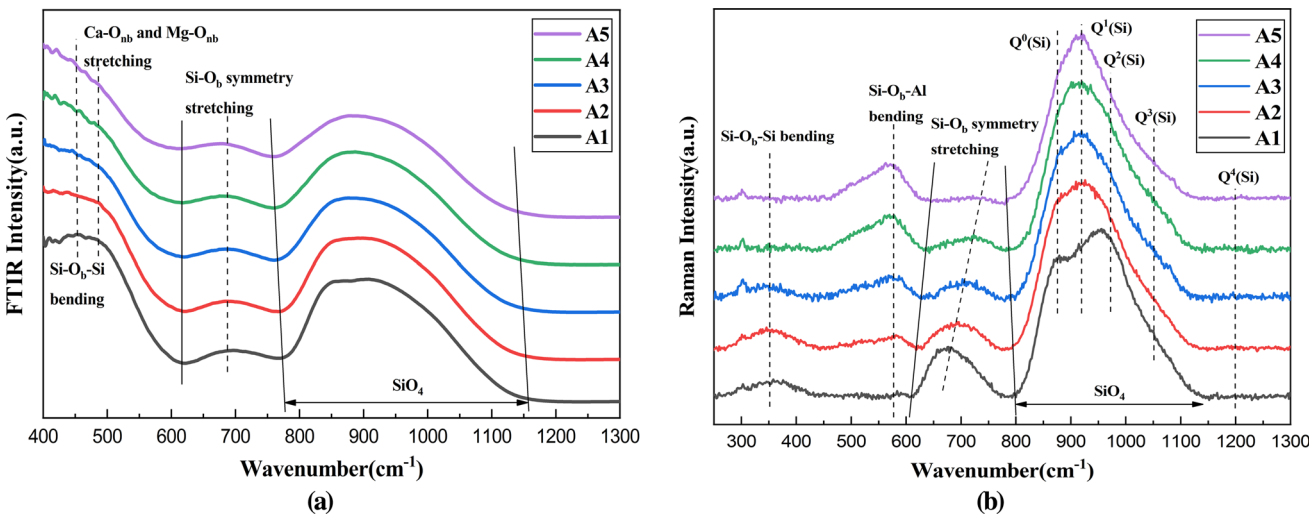

Fig. 5—FTIR and Raman spectra of the prepared glassy samples: (*a*) FTIR and (*b*) Raman.

content was higher. It could be preliminarily speculated that the incremental Al_2O_3 concentration might reduce the content of Q^0(Si) and Q^2(Si) but generate more Q^1(Si) in the network.

Careful fitting of Raman curves in the high-frequency region allows us to quantitatively investigate the Si-related structure. Many previous studies[17,33,34] indicated the centers of bands related to Q^0(Si), Q^1(Si), Q^2(Si), Q^3(Si) and Q^4(Si) were located at ~ 870, ~ 910, ~ 970, ~ 1050 and ~ 1200 cm^{-1}, respectively. There was no detectable peak at ~ 1200 cm^{-1}, and the fitting curves should be focused on the obvious peaks or shoulders. Hence, four Gaussian functions assigned the four Q^i(Si) (i = 0, 1, 2 and 3) were used to fit the Raman spectra in the range of 800 to 1150 cm^{-1}. Gaussian fittings to these various Raman curves are shown in Figures 6(a) through (e). Based on the band areas of the fitted Gaussian curve, namely A_i (i = 0, 1, 2 and 3) corresponding to Q^i(Si) (i = 0, 1, 2 and 3), the mole fractions of various Q^i(Si) could be calculated from the following equation:

$$X_i = (A_i/S_i) \Big/ \left(\sum_{i=0}^{3} A_i/S_i \right) \quad [1]$$

where X_i, A_i and S_i denote the mole fraction, band area and Raman scattering coefficient of Q^i(Si), respectively. The values of S_0, S_1, S_2 and S_3 are equal to 1, 0.514, 0.242 and 0.09, respectively.[35] The variation trend of mole fractions of various Q^i(Si) with increasing Al_2O_3 content is presented in Figure 6(f), as will be discussed later.

2. ^{27}Al MAS-NMR spectra

To further identify the roles of Al in the network, the ^{27}Al MAS-NMR spectra of prepared glassy samples were collected and are plotted in Figure 7. The resonance of Al-related units occurred between − 20 and 100 ppm, and all the resonance peaks were similar with a dominant peak at ~ 60 ppm. According to the previous research,[22] the main resonance appearing at 50 to 65 ppm was characteristic of the presence of fourfold coordinated Al^{3+} (AlO_4), while the secondary resonance at 0 to 40 ppm indicated the presence of fivefold coordinated Al^{3+} (AlO_5) and sixfold coordinated Al^{3+} (AlO_6). These three different sorts of Al-related units represented the complex roles of Al in the glass network, which directly determined the amphoteric behavior of Al_2O_3. As shown, the main peak and FWHM (full width at half maximum) of each curve are marked in Figure 7. It could be observed that with Al_2O_3 added, there was no significant shift in the position of the main peak when the FWHM continuously extended outwards from the main peak, which meant the degree of disorder of the aluminum resonance increased. For a change in the quantity of Al-related units, it could be correspondingly speculated that with increasing Al_2O_3 content, the AlO_4 concentration gradually decreased and the concentration of AlO_5 and AlO_6 increased.

To further obtain the different proportions of the three Al-related units in the networks, deconvolution of the ^{27}Al MAS-NMR curves was performed in the region of − 20 to 100 ppm. It was reported that the resonant centers of AlO_4, AlO_5 and AlO_6 were located at ~ 60, ~ 40 and ~ 10 ppm, respectively.[11,17] Hence, three Gaussian functions assigned to the three AlO_i species

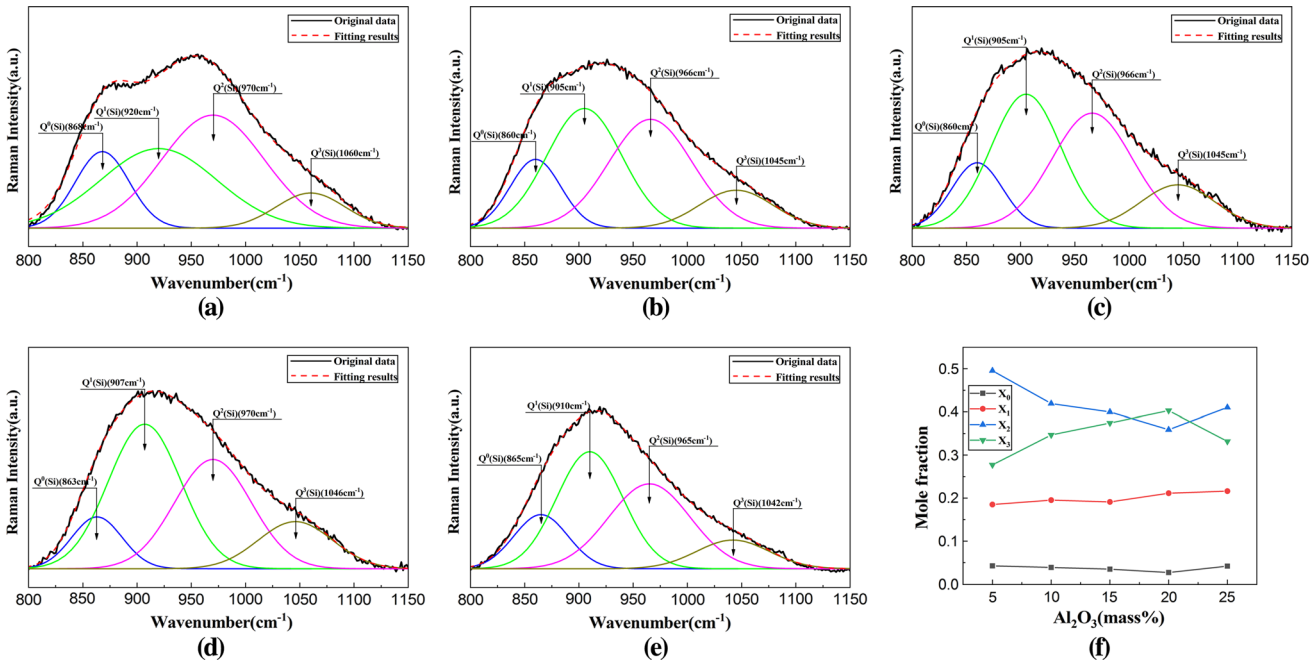

Fig. 6—Fitting results of Raman spectra in the 800 to 1150 cm^{-1} wavenumber range with Gaussian functions of (*a*) sample A1, (*b*) sample A2, (*c*) sample A3, (*d*) sample A4, (*e*) sample A5 and (*f*) mole fractions of various Q^i(Si) (i = 0, 1, 2 and 3).

(i = 4, 5 and 6) were used to fit the NMR spectra. Gaussian fittings to these curves are shown in Figures 8(a) to (e). Based on the band areas of the fitted Gaussian curve, the mole fractions of various Al-related units could be calculated from the following equation:

$$X_{\mathrm{AlO}_i} = A_{\mathrm{AlO}_i} \Big/ \left(\sum_{i=4}^{6} A_{\mathrm{AlO}_i} \right) \quad [2]$$

where X_{AlO_i} and A_{AlO_i} denote the mole fraction and band area of $\mathrm{AlO_i}$, respectively. The variation trend of mole fractions of various $\mathrm{AlO_i}$ with incremental Al_2O_3 content is shown in Figure 8(f), as will be discussed in the following section.

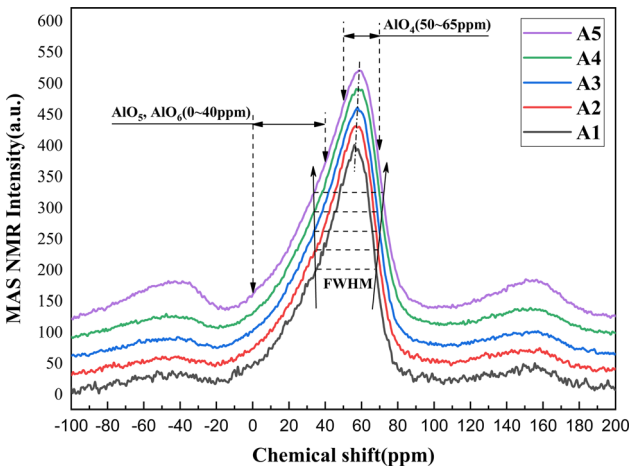

Fig. 7—^{27}Al MAS-NMR spectra of the prepared glassy samples.

C. *Relationship Between the Viscosity and Structure of Molten Slags*

1. *Quantitative relationship between the viscosity and structure*

As mentioned before, the variational composition of the slag melt affects the macroscopic properties relying on the change in structure at the micro-level. Therefore, to understand the relationship between viscosity and structure, two aspects, compositional effects on structure and structural effects on viscosity, need to be clarified.

The compositional effects on the major structure of Si- and Al-related units are illustrated in Figures 6(f) and 8(f), respectively. As shown in Figure 6(f), at the initial stage of Al_2O_3 addition, the mole fractions of Q^1(Si) and Q^3(Si) species both increased at the cost of Q^0(Si) and Q^2(Si) species. This structural transformation responsible for the increase of the DOP of the network indicated that Al_2O_3 played a primary role as a network-forming oxide as a whole. From the conventional perspective, for the aluminosilicate glass structure, O_{nb} in SiO_4 tetrahedra converted into O_b in Si-O_b-Al with AlO_4 tetrahedra introduced into the silicate network, which is shown in Figure 9(a). Although AlO_4 might interact with any kind of SiO_4 tetrahedra containing O_{nb} in theory, here Q^0(Si) and Q^2(Si) species were notably consumed because of high levels of O_{nb} for Q^0(Si) and the dominant proportion for Q^2(Si). As Al_2O_3 was further added, the Q^3(Si) species transformed into lower O_b number species of Q^0(Si), Q^1(Si)and Q^2(Si). This indicated that the network structure began to depolymerize and the role of Al_2O_3 transformed into a network modifier overall. In other words, the high-coordinate

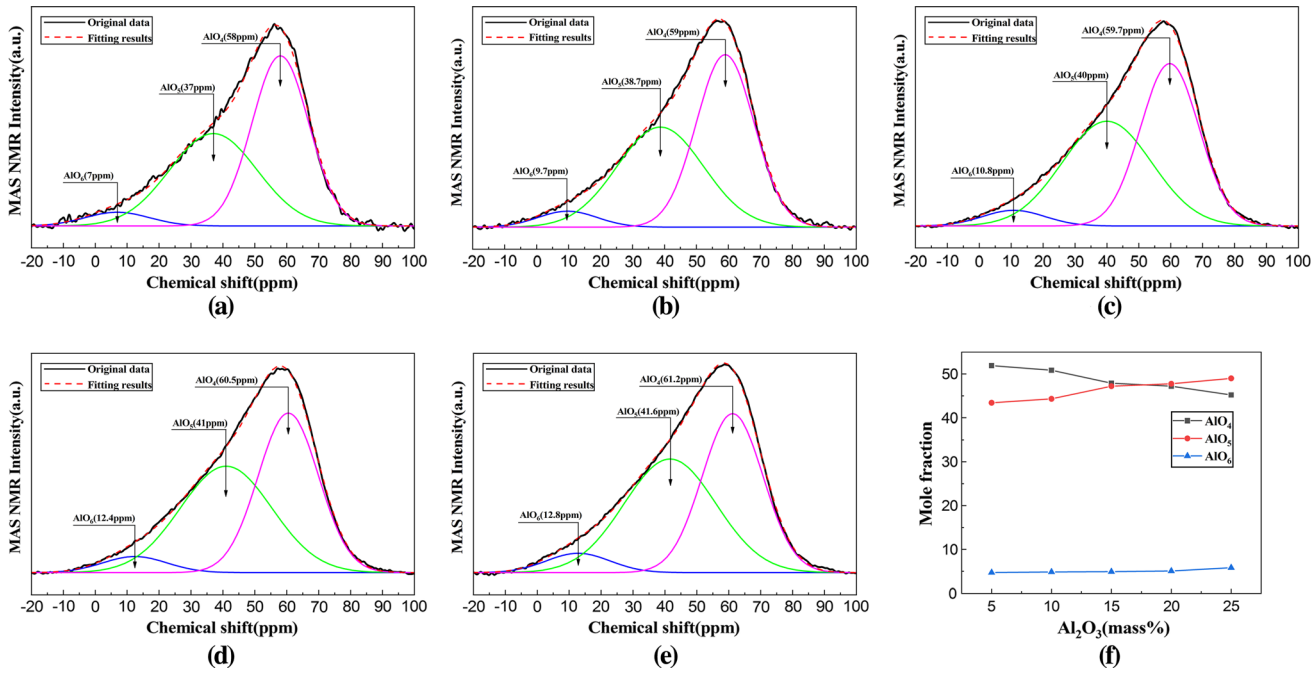

Fig. 8—Fitting results of ^{27}Al MAS-NMR spectra in the chemical shift range of 800 to 1150 ppm with Gaussian functions of (*a*) sample A1, (*b*) sample A2, (*c*) sample A3, (*d*) sample A4, (*e*) sample A5 and (*f*) mole fractions of various Al-related structure units (i = 0, 1, 2 and 3).

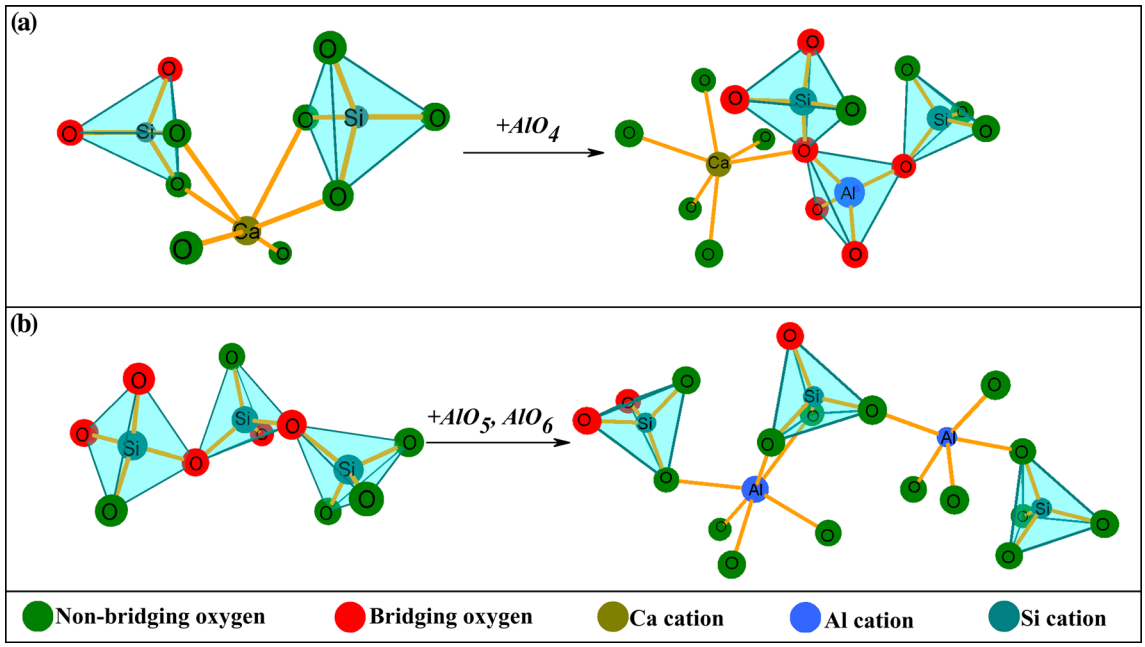

Fig. 9—Schematic illustration of the roles of different Al-related units: (*a*) AlO_4, (*b*) AlO_5 and AlO_6 in the network structure.

units of Al, namely, AlO_5 and AlO_6, began to present a more significant influence on the network structure, and their depolymerization behavior was vividly illustrated in Figure 9(b).

Additionally, Figure 8(f) demonstrated that the mole ratio of AlO_5/AlO_4 increased with increasing Al_2O_3 content, which could likewise confirm the role change of Al_2O_3. The result that the average coordination number of Al gradually increased was also consistent with previous studies.[9,17,31] First, the residual charge numbers on the oxygen of AlO_5, AlO_5 and AlO_6 could be clearly compared when they were expressed as $[O\text{-}Al_{1/4}]^{-5/4}$, $[O\text{-}3Al_{1/5}]^{-1/5}$ and $[O\text{-}4Al_{1/6}]^{0}$, respectively,[31] and were apparently decreased successively. Second, the concentration of alkali-earth metal cations was lowered with incremental Al_2O_3 content, and as a consequence, the compensation charges were gradually reduced. Therefore, high-coordinated Al units with fewer residual charges were more likely to form because of the limited quantity of compensation charges in the networks.

As for the structural effects on viscosity, they could be analyzed based on the shifty DOP of the network. As recognized, a higher DOP tended to lead to a higher viscosity. For the purpose of quantitatively analyzing the relationship between viscosity and structure, the average number of O_{nb} per coordinated network forming atom, which was denoted as (NBO/*T*), was used to quantify the DOP of the glassy network. In detail, for the silicate network structure, the value of (NBO/*T*) could be computed by Eq. [3]. Herein, considering the effects of partial Al_2O_3 likewise as a network former, the modified (NBO/*T*) denoted as (NBO/*T*)′ was employed and could be obtained by Eq. [4].

$$\mathrm{NBO}/T = \sum_{i=0}^{4}(4-i)\cdot X_i \qquad [3]$$

$$(\mathrm{NBO}/T)' = \frac{x_{\mathrm{SiO_2}}\cdot\sum_{i=0}^{4}(4-i)\cdot X_i}{x_{\mathrm{SiO_2}} + 2x_{\mathrm{Al_2O_3}}\cdot b\cdot X_{\mathrm{AlO_4}}} \qquad [4]$$

Here x_{SiO_2} and $x_{Al_2O_3}$ are the molar contents of SiO_2 and Al_2O_3 in the sample, respectively; *b* is the ratio of cationic field strengths (Z_c/r^2, where Z_c and *r* are the valence and radius of the cation, respectively) of Al^{3+} and Si^{4+}, and its value is 0.427.[36]

Figure 10(a) presents the calculation results of (NBO/*T*)′ in the molten slags at high temperature. As expected, the value of (NBO/*T*)′ decreased first and then increased with Al_2O_3 gradually added, also indicating that there were two stages of changes in the slag structure. In the first stage, the simple anion clusters in the melt were connected in a complex network structure by AlO_4 tetrahedra. Therefore, the friction between the ions increased and the viscosity increased correspondingly. In the second stage, the complex network structure was broken by AlO_5 and AlO_6. Therefore, the friction between the ions decreased, and the viscosity decreased correspondingly. This could felicitously explain the discontinuous variation tendency of melt viscosity at

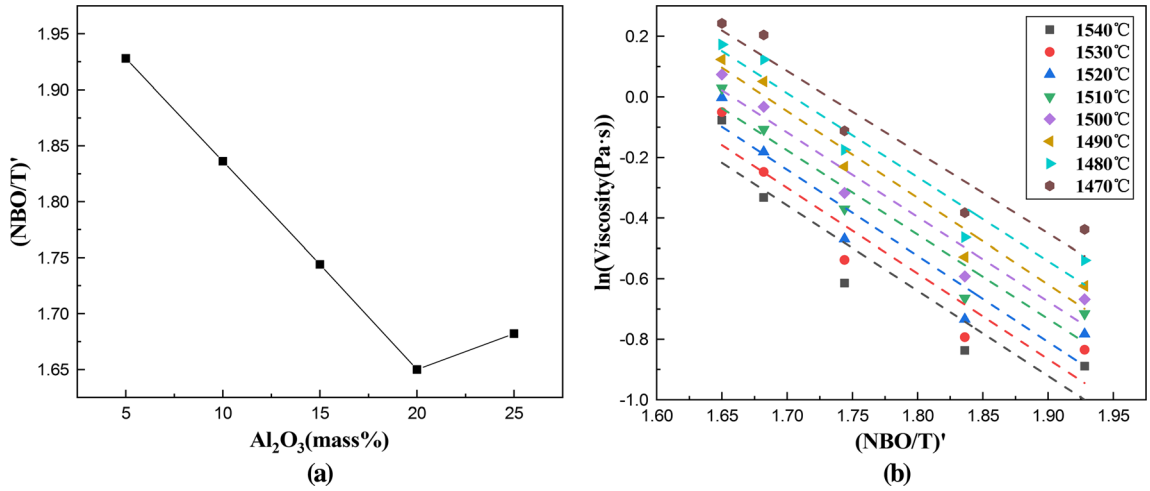

Fig. 10—Value changes of (NBO/T)′ with increasing Al_2O_3 content (*a*) and the relation between viscosities and (NBO/T)′ (*b*) in molten slags at high temperatures.

high temperature and simultaneously confirm the amphoteric behavior of Al_2O_3 on viscosity at the microstructural level.

Figure 10(b) shows the linear fitting results of the logarithm of viscosity and (NBO/T)′ at the temperature range of 1470 °C to 1540 °C. As can be seen, with increasing (NBO/T)′, the logarithm of viscosity gradually decreased, which was in accordance with the above analyses. The result was also consistent with previous studies. For example, Tang *et al.*[36] confirmed the negative correlation between the logarithm of viscosity and (NBO/T), and Wu *et al.*[37] also found a fine linear correlation between the logarithm of viscosity and (NBO/T) of the CaO-SiO_2 system. Here, the functional relationship between viscosity and (NBO/T)′ can be expressed as Eq. [5]:

$$\ln(\text{Viscosity}) = a + b \cdot (NBO/T)' \quad [5]$$

The values of a, b and the coefficient of determination R^2 are displayed in Table II. It can be observed that, on the whole, a fine linear correlation was exhibited between the logarithm of viscosity and (NBO/T)′. This clearly indicated the quantitative relationship among the viscosity, temperature and microstructures of slags.

2. *Viscosity and Structure Analysis—Thermodynamic View*

In this section, activity coefficients and Gibbs free energy were taken into account to analyze the viscosity and structure from the thermodynamic view. Activity coefficients (γ_i) and molar excess Gibbs free energy $\left(\Delta_{\text{mix}}G_m^E\right)$ can exhibit deviations from the ideal behavior, and the molar Gibbs free energy of real mixing $\left(\Delta_{\text{mix}}G_m^{re}\right)$ can reflect the stability of the slag system.[38–40] Here, the activity values (a_i) were calculated by FactSage 7.1. The values of γ_i, $\Delta_{\text{mix}}G_m^E$ and $\Delta_{\text{mix}}G_m^{re}$ can be obtained from the following equations:

$$\gamma_i = a_i/x_i \quad [6]$$

$$\Delta_{\text{mix}}G_m^E = RT\sum_{i=1}^{m} x_i \ln \gamma_i \quad [7]$$

$$\Delta_{\text{mix}}G_m^{re} = RT\sum_{i=1}^{m} x_i \ln a_i \quad [8]$$

The activity coefficient of Al_2O_3 at 1540 °C and its first derivative are exhibited in Figure 11(a). It can be seen that the activity coefficient displayed a negative deviation from the ideal state. It was interesting to note that with increasing Al_2O_3 content, the activity coefficient of Al_2O_3 gradually increased at a discontinuous rate and its growth trajectory approximated an "S" curve. The transition point of the "S" curve appeared at about 17 wt pct Al_2O_3 content, where the first derivative reached its maximum. This signified the role of Al_2O_3 in the structure, and the viscosity changed at this point. When the Al_2O_3 content was < 17 wt pct, Al ions were preferentially introduced into the voids in the silicate networks to form AlO_4 tetrahedra with the consumption of NBO. However, this was restrained by less and less O_{nb} until Al ions in the network reached saturation. As a result, the inhibiting effect on the activity coefficient of Al_2O_3 was gradually weakened because of subdued interactions between Al_2O_3 and SiO_2, and the activity coefficient of Al_2O_3

Table II. Linear Fitting Function and Coefficient of Determination R^2 of ln(Viscosity) and (NBO/T)′ at High Temperature

Temperature (°C)	1540	1530	1520	1510	1500	1490	1480	1470
a	4.43 ± 1.09	4.50 ± 0.99	4.59 ± 0.92	4.55 ± 0.78	4.62 ± 0.72	4.81 ± 0.64	4.72 ± 0.70	4.63 ± 0.78
b	− 2.81 ± 0.62	− 2.83 ± 0.56	− 2.84 ± 0.52	− 2.78 ± 0.44	− 2.79 ± 0.41	− 2.86 ± 0.36	− 2.77 ± 0.40	− 2.68 ± 0.44
R^2	0.8745	0.8958	0.9080	0.9288	0.9394	0.9546	0.9423	0.9252

increased with a gradual and accelerating trend. When the Al_2O_3 content was > 17 wt pct, because there was not enough cationic charge in the networks, a mass of AlO_5 and AlO_6 units with less residual charges formed. They showed another kind of interaction with SiO_2 and depolymerized the network. Hence, the inhibiting effect on the activity coefficient of Al_2O_3 was strengthened, and the activity coefficient of Al_2O_3 increased with a gradually slowing trend.

Figure 11(b) presents the variation of the molar Gibbs free energy of real mixing and molar excess Gibbs free energy of the CaO-SiO_2-MgO-Al_2O_3 system at 1540 °C with incremental Al_2O_3 content. It can be seen that the system with about 17 wt pct Al_2O_3 content possessed a minimum molar Gibbs free energy of real mixing. According to the analysis of the phase diagram in Figure 1, this composition point lay on the intersecting line of two primary crystal regions, merwinite and gehlenite. Although the relationship of the primary phase and melt structure was unclear, it could be speculated that two different types of structure changes existed. Regarding the molar excess Gibbs free energy of the system, it also possessed a minimum value but at a lower Al_2O_3 concentration of about 8 wt pct. Figure 11(a) shows that before this composition, the activity coefficient of Al_2O_3 remained a fairly small value. This indicated that a dramatic deviation from the ideal state had been caused owing to the formation of AlO_4 tetrahedra and reached its maximum at the composition of about 8 wt pct Al_2O_3 content, namely, molar excess Gibbs free energy reached the minimum value.

The analysis above, in fact, confirmed two different and important types of structural changes at different Al_2O_3 concentration ranges from the thermodynamic view, and the viscosity variation actually originated from the structure changes. This is basically consistent with the experimental results of the viscosity and structures.

IV. CONCLUSION

This study gained insight into the relationship between the viscosity and structure of CaO-SiO_2-MgO-Al_2O_3 molten slags. Viscosity and structure, as well as their relationship, were quantitatively studied. Also, the amphoteric behavior of Al_2O_3 on the structure and viscosity was confirmed from the thermodynamic view. The following conclusions could be drawn here:

(1) The results of slag viscosity indicated there was an amphoteric behavior of Al_2O_3 on the viscosity at high temperature > 1460 °C, and the slag viscosity reached the maximum as the Al_2O_3 content was 20 wt pct.
(2) The Si-related unites identified by FTIR and Raman fitting showed a discontinuous change. At the initial stage of Al_2O_3 addition, the mole fractions of Q^1(Si) and Q^3(Si) species both increased at the cost of Q^0(Si) and Q^2(Si) species. As Al_2O_3 was further

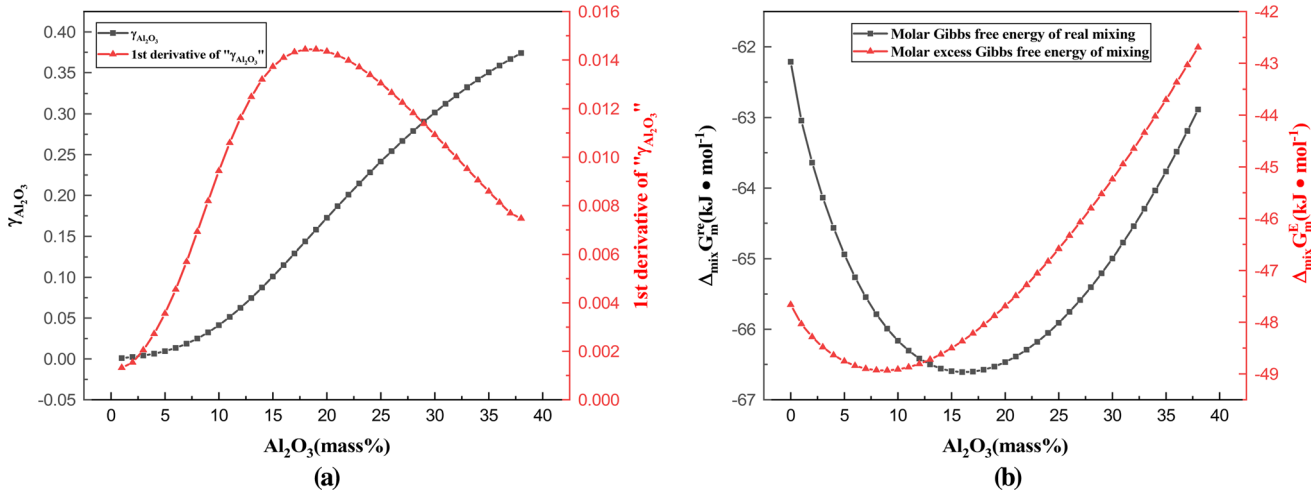

Fig. 11—Change of thermodynamic properties of CaO-SiO_2-MgO-Al_2O_3 molten slags at 1540 °C with the concentration of Al_2O_3: (*a*) the activity coefficient of Al_2O_3 and its first derivative (*b*) molar Gibbs free energy of real mixing and molar excess Gibbs free energy of mixing.

added, the Q^3(Si) species transformed into lower O_b number species of Q^0(Si), Q^1(Si) and Q^2(Si).

(3) The fitting results of ^{27}Al MAS-NMR spectra indicated that AlO_4, AlO_5 and AlO_6 existed in the networks. High-coordinated Al units with fewer residual charges (AlO_5 or AlO_6) were more likely to form with increasing Al_2O_3 content, which drove the shift of the Al_2O_3 role from a network former to a network modifier.

(4) DOP of glassy networks quantified by $(NBO/T)'$ increased first, followed by a decrement, and reached a maximum as the Al_2O_3 content was 20 wt pct. Through the thermodynamic analysis, the transition point in structure and viscosity was at the composition of about 17 wt pct Al_2O_3, which was close to the experimental result.

ACKNOWLEDGMENTS

Support from the National Key Research and Development Project of China (2018YFC1901505) is acknowledged. This work was also supported by the National Natural Science Foundation of China (51672006 and 51472006) and the Ministry of Land and Resources Public Welfare Industry Research Project (201511062-02).

REFERENCES

1. M. Yellishetty and G.M. Mudd: *J. Clean Prod.*, 2014, vol. 84, pp. 400–10.
2. Z. Yan, X. Lv, J. Zhang, Y. Qin, and C. Bai: *Can. Metall. Q.*, 2016, vol. 55, pp. 186–94.
3. M. Thangavelu and A.K. Bhattacharya: *J. Indian Soc. Remote Sens.*, 2011, vol. 39, pp. 473–83.
4. D. Liu, H. Liu, J. Zhang, Z. Liu, X. Xue, G. Wang, and Q. Kang: *Int. J. Miner. Metall. Mater.*, 2017, vol. 24, pp. 991–98.
5. A.S. Mehta and V. Sahajwalla: *Scand. J. Metall.*, 2010, vol. 29, pp. 17–29.
6. W.H. Kim, I. Sohn, and D.J. Min: *Steel Res. Int.*, 2010, vol. 81, pp. 735–41.
7. N. Saito, N. Hori, K. Nakashima, and K. Mori: *Metall. Mater. Trans. B*, 2003, vol. 34B, pp. 509–16.
8. Y. Gao, S. Wang, C. Hong, X. Ma, and Y. Fu: *Int. J. Miner. Metall. Mater.*, 2014, vol. 21, pp. 353–62.
9. J.F. Stebbins, E.V. Dubinsky, K. Kanehashi, and K.E. Kelsey: *Geochim. Cosmochim. Acta*, 2008, vol. 72, pp. 910–25.
10. B. Hehlen and D.R. Neuville: *J. Phys. Chem. B*, 2015, vol. 119, pp. 4093–98.
11. C.L. Losq, D.R. Neuville, P. Florian, G.S. Henderson, and D. Massiot: *Geochim. Cosmochim. Acta*, 2014, vol. 126, pp. 495–17.
12. Z. Wang, Y. Sun, S. Sridhar, Z. Mei, G. Min, and Z. Zhang: *Metall. Mater. Trans. B*, 2015, vol. 46B, pp. 537–41.
13. Y. Lu, R. Shan, X. Wang, Q. Liu, L. Dong, J. Yang, and J. Liu: *Steel Res. Int.*, 2016, vol. 87, pp. 241–49.
14. G.H. Kim and I. Sohn: *J. Non-Cryst. Solids*, 2012, vol. 358, pp. 1530–37.
15. F. Cong, M. Chu, J. Tang, Y. Tang, and Z. Liu: *Steel Res. Int.*, 2016, vol. 87, pp. 1274–83.
16. H. Kim, H. Matsuura, F. Tsukihashi, W. Wang, J.M. Dong, and I. Sohn: *Metall. Mater. Trans. B*, 2013, vol. 44B, pp. 5–12.
17. Y. Sun, H. Wang, and Z. Zhang: *Metall. Mater. Trans. B*, 2018, vol. 49B, pp. 677–87.
18. J.H. Park, J.M. Dong, and H.S. Song: *Metall. Mater. Trans. B*, 2004, vol. 35B, pp. 269–75.
19. C. Sun, X. Liu, J. Li, X. Yin, S. Song, and Q. Wang: *ISIJ Int.*, 2017, vol. 57, pp. 578–82.
20. J.H. Park, H. Kim, and J.M. Dong: *Metall. Mater. Trans. B*, 2008, vol. 39B, pp. 150–53.
21. A. Aronne, S. Esposito, and P. Pernice: *Mater. Chem. Phys.*, 1997, vol. 51, pp. 163–68.
22. F. Wang, A. Stamboulis, D. Holland, S. Matsuya, and P. Layrolle: *Key Eng. Mater.*, 2008, vols. 361–363, pp. 825–28.
23. H. Li, H. Li, and W. Li: *Coal Sci. Technol.*, 2006, vol. 34, pp. 24–26.
24. B.N. Roy: *J. Am. Ceram. Soc.*, 2010, vol. 73, pp. 846–55.
25. N.J. Clayden, S. Esposito, A. Aronne, and P. Pernice: *J. Non-Cryst. Solids*, 1999, vol. 258, pp. 11–19.
26. Y. Sun and Z. Zhang: *Metall. Mater. Trans. B*, 2015, vol. 46B, pp. 1549–54.
27. P. Lu, W. Xia, H. Jiang, and H. Zhao: *Bull. Chin. Ceram. Soc.*, 2015, vol. 34, pp. 878–87.
28. Y. Jiang, X. Lin, K. Ideta, H. Takebe, M. Jin, S.H. Yoon, and I. Mochida: *J. Ind. Eng. Chem.*, 2014, vol. 20, pp. 1338–45.
29. S. Markovic, V. Dondur, and R. Dimitrijevic: *J. Mol. Struct.*, 2003, vol. 654, pp. 223–34.
30. I. Daniel, P. Gillet, B.T. Poe, and P.F. Mcmillan: *Phys. Chem. Miner.*, 1995, vol. 22, pp. 74–86.
31. J. Stebbins: *Chem. Geol.*, 2013, vol. 346, pp. 34–46.

32. T. Takaishi, M. Kato, and K. Itabashi: *J. Phys. Chem.*, 1994, vol. 98, pp. 5742–43.
33. G. Jiang, J. You, Y. Wu, H. Hou, and H. Chen: *Geol.-Geochem.*, 2003, vol. 31, pp. 80–86.
34. W. Wang, J. Tan, D. Zhang, Q. Wang, J. Tian, and S. Tian: *J. Earth Sci.*, 2004, vol. 29, pp. 39–44.
35. Y. Wu, G. Jiang, J. You, H. Hou, and H. Chen: *Acta Phys. Sin.*, 2005, vol. 54, pp. 961–66.
36. X. Tang, M. Guo, X. Wang, Z. Zhang, and M. Zhang: *J. Univ. Sci. Technol. Beijing*, 2010, vol. 32, pp. 1542–46.
37. T. Wu, S. He, Y. Liang, and Q. Wang: *J. Non-Cryst. Solids*, 2015, vol. 411, pp. 145–51.
38. V.L. Stolyarova: *J. Non-Cryst. Solids*, 2008, vol. 354, pp. 1373–77.
39. Q. Shu, P. Li, X. Zhang, and K. Chou: *Metall. Mater. Trans. B*, 2016, vol. 47B, pp. 1–6.
40. A. Shankar, M. Görnerup, A.K. Lahiri, and S. Seetharaman: *Metall. Mater. Trans. B*, 2007, vol. 38B, pp. 911–15.